Rover Operations for Subsurface Mining on the Moon

Alex Ellery [(1)], Mark Schwarz [(1)], Pablo Molina Cabreira [(1)], Brian Lynch [(1)], Cameron Frazier [(1)], Adam Mack [(1)]

[(1)] Department of Mechanical & Aerospace Engineering, Carleton University, 1125 Colonel By Drive, Ottawa, ON. K1S 5B6. CANADA, Email: aellery@mae.carleton.ca

ABSTRACT

Subsurface mines on the Moon will be necessary to access buried asteroidal material to supplement indigenous lunar resources for in-situ resource utilization (ISRU). These resources will be essential for industrialisation of the Moon. Rover operations in such mines are subject to particular constraints that are addressed – slope-dependent slippage, computational limits in visual simultaneous localisation and mapping (SLAM) and path planning in cluttered environments. Although there are challenges, these issues can be addressed enhancing the feasibility of subsurface lunar mining.

1. INTRODUCTION

Lunar mining of in-situ resources has emerged as an enabling technology for the next phase of space exploration. We focus on the mining of non-volatile resources for the extraction of ceramics, glasses and metals for the construction of a durable and sustainable lunar infrastructure (Appendix: Table 1) [1]. The resources currently targeted are the common rock-forming minerals of the Moon – plagioclase feldspars, pyroxenes, olivine and ilmenite. In particular, the extraction of aluminium from lunar anorthite and iron-titanium from lunar ilmenite are the primary source of bulk lunar metals. Although metals in pure form have utility, the functional versatility of metals are embodied in their alloy range. It is essential that the inventory of lunar resources is enhanced by supplemental asteroidal material, especially nickel-iron classes which offer alloying materials Ni, Co and, more sparingly, W. This would extend the range of alloys manufacturable on the Moon dramatically sufficient to provide a functional range to construct all onboard spacecraft functions (Appendix: Table 2). It is estimated that there are considerable NiFe resources that have been delivered to the Moon by meteoritic bombardment over the aeons residing on the surface or under the surface of shallow-angle impact craters [2]. Strong magnetic anomalies at the northern rim of the south pole Aitken basin may be due to impact-delivered magnetic iron [3,4]. On the assumption that such ores reside beneath the surface buried due to subsequent impact gardening, we must access such resources through tunnelling. Low-inclination descending tunnelling to access such subsurface ores reduce the energy imposed by extensive overburden removal during quarrying. We assume that construction of the mine through blasthole drilling, blasting and rock fragment removal by loader-haul-dumpers have been undertaken and that ore mining is through mechanized cut-and-filling.

We discuss several issues regarding underground rover operations inherent in such mines. All rover control issues boil down to slippage that we examine first by simulating a slip prediction algorithm. Slip is the most significant error that must be accounted for in SLAM (simultaneous localization and mapping), the process of self-localisation of position and orientation with respect to landmarks within a map representation of the local environment. The second issue we address is that of visual navigation as part of SLAM, paying special emphasis on computational issues imposed by limited computational resources onboard mining rovers. It is from SLAM that path planning is enabled. Thirdly, we examine artificial potential fields for path planning by adopting exponentially decreasing functions to cope with highly cluttered environments expected within a mine.

2. PROBLEM OF SLIPPAGE

Slope-dependent slip is inherent in this type of environment within which an inclined mining tunnel slopes towards a submerged ore body. One such slip model is the polynomial Lindmann-Voorhees slip model constructed from experiments with a Mars Exploration Rover flight spare on Mars-like sandy terrain [5]:

$$s_x = -1696e^{-6}\phi^6 - 2.402e^{-5}\phi^5 + 7.985e^{-4}\phi^4$$
$$+ 1.805e^{-3}\phi^3 - 1.471e^{-2}\phi^2$$
$$+ 2.319e^{-1}\phi + 1.753$$
$$s_y = 2.361e^{-4}\theta^4 + 5.128e^{-2}\theta^2 + 1.471$$
$$s_\psi = 0$$

where φ, θ=slope in that direction (longitudinal in the direction of travel x, lateral y and yaw direction ψ) which yield control inputs $u_k = (\phi \quad \theta)^T$. Without accommodation of slip, the rover path will cumulatively grow errors (Fig 1). We have developed a slip-adaptive rover navigation algorithm that adapts a rover state transition model to compensate for rover slip. A three-layer multilayer perceptron learns to model slip as the rover traverses the simulated terrain with 3 input neurons, n hidden neurons and 3 output neurons (20 hidden neurons was selected as a trade between accuracy and learning time). An extended Kalman filter (EKF) estimates rover localisation using a kinematic model with wheel odometry measurements:

$$q_k = \begin{pmatrix} x_k \\ y_k \\ \psi_k \end{pmatrix} = \begin{pmatrix} c\psi_{k-1}c\phi_k\Delta t & 0 \\ s\psi_{k-1}c\phi_k\Delta t & 0 \\ 0 & \Delta t \end{pmatrix} \begin{pmatrix} v_k \\ w_k \end{pmatrix} + \begin{pmatrix} x_{k-1} \\ y_{k-1} \\ \psi_{k-1} \end{pmatrix} + w_k$$

$$z_k = h(q_k) + v_k$$

$$h_{ik} = \begin{pmatrix} r_i \\ \beta_i \end{pmatrix} = \begin{pmatrix} \sqrt{(x_i - x_k)^2 + (y_i - y_k)^2} \\ arctan2\left(\dfrac{y_i - y_k}{x_i - x_k}\right) - \psi_k \end{pmatrix}$$

where $q_k = (x_k \quad y_k \quad \psi_k)^T$=rover state of x,y position and yaw ψ about the z-axis, Δt=sample time, $c\theta$=$\cos\theta$, $s\theta$=$\sin\theta$, v=rover velocity, w=rover angular velocity, w_k=Gaussian process noise, r_i=range of landmark i, β_i=bearing to landmark i, $h_{ik} = (r_i \quad \beta_i)^T$=measurement vector of ith feature, $(x_i \quad y_i)$=planar cartesian coordinates of the ith feature, v_k=Gaussian measurement noise. We have also adopted the EKF as the neural network learning rule which incorporates information from previous training data for enhanced convergence rate over backpropagation. The extended Kalman model is a state transition function augmented with slip

referenced to global map coordinates.

$$\begin{pmatrix} x_k \\ y_k \\ \psi_k \\ W_k \end{pmatrix} = \begin{pmatrix} c\psi_{k-1}c\phi_k\Delta t & 0 \\ s\psi_{k-1}c\phi_k\Delta t & 0 \\ 0 & \Delta t \\ 0 & 0 \end{pmatrix}\begin{pmatrix} v_k \\ w_k \end{pmatrix}$$
$$+ \begin{pmatrix} x_{k-1} \\ y_{k-1} \\ \psi_{k-1} \\ W_{k-1} \end{pmatrix} - \begin{pmatrix} s_{x,k}c\psi c\phi + s_{y,k}c\psi s\phi s\theta - s\psi c\theta \\ s_{x,k}s\psi c\phi + s_{y,k}s\psi s\phi s\theta + c\psi c\theta \\ s_{\psi,k} \\ 0 \end{pmatrix}$$

Simulation of the slip-adaptive algorithm shows that the neural network learned the simulated slip giving errors <30 cm within the 3σ error bounds (Fig 2).
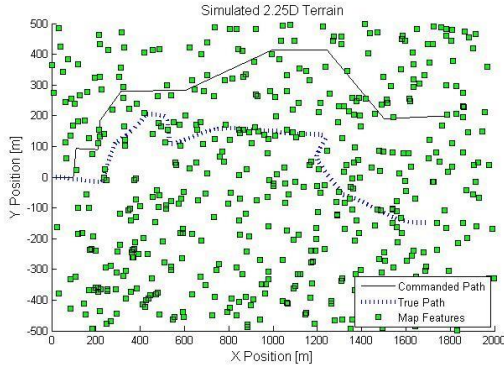

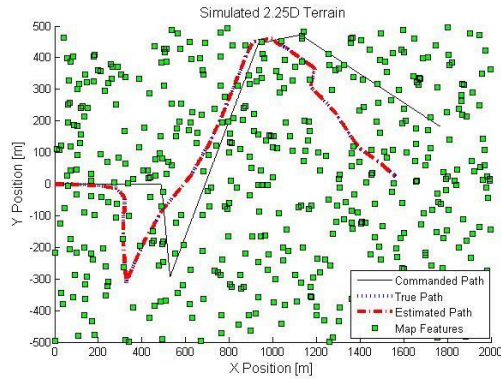Figure 1. Rover deviation from commanded path due to slip

Figure 2. Rover path with slip prediction

3. COMPUTATIONAL IMPLICATIONS OF VISUAL MAPBUILDING

Simultaneous localization and mapbuilding (SLAM) is the process of rover self-localisation with respect to external landmarks [6]. An indoor area was adopted to approximate to a lunar excavated tunnel environment characterised by confining walls and populated by objects and structures (Fig 3).
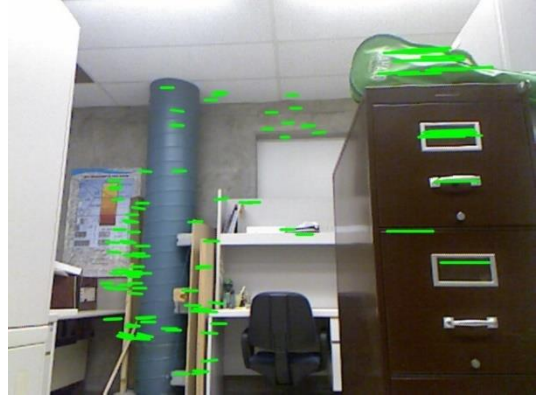

Figure 3. Indoor environment emulating cluttered mining tunnel

A Husky rover-mounted Kinect camera with RGB-D (red-green-blue-depth) capabilities was deployed to perform visual navigation. Planetary rovers employ onboard computers with limited capacity so it is essential to employ computationally-efficient algorithms. An unscented Kalman filter was adopted to yield sample (sigma) points to represent probability distribution mean and error covariance [7]. The front end of visual SLAM is responsible for motion estimation between current and previous image frames. Such visual odometry requires tracking visual features extracted from the images. We tested several feature detection algorithms that extract features including depth. These involve computationally intensive feature descriptors such as scale-invariant feature transform (SIFT) [8] and speeded up robust features (SURF) [9] and both yield similar performance. Features from accelerated segment test (FAST) is a faster algorithm [10]. Binary robust invariant scalable keypoints (BRISK) [11] and oriented FAST and Rotated BRIEF (ORB) [12] feature descriptors offer adaptive steps and even more computational efficiency. BRISK and ORB feature descriptors offer higher computational efficiency than SURF and SIFT by almost an order of magnitude. We found that BRISK performs better than ORB but with a similar computational load (Fig 4).
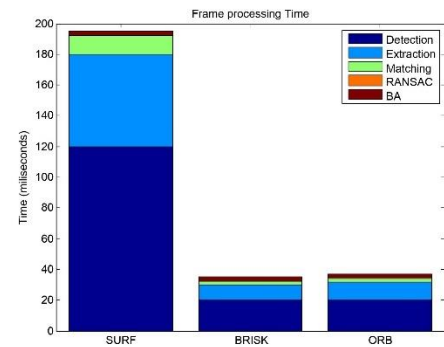

Figure 4. Computational processing times for different front end SLAM algorithms (RANSAC=random sample consensus, BA=bundle adjustment)

The Freidburg dataset was used for testing BRISK performance [13,14] (Fig 5).
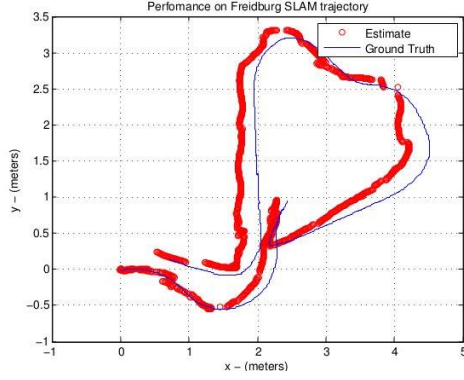
Figure 5. Roundtrip Freidburg SLAM trajectory using BRISK

Recalibration offered by loop closure at the end of the traverse returning to near its start position shows that recalibration may be employed for multiple traverses through a mining tunnel to a submerged ore face.

4. POTENTIAL FIELD PATH PLANNING

We explore the use of exponential potential fields to provide autonomous navigation through very narrow corridors and obstacles characteristic of mining tunnels and shafts and multirover coordination. The reactive vector equilibrium (RAVE) approach presented here resolves many problems associated with potential fields by imposing supplementary potential fields which impose risk and tangential forces [15]:

$$F_{rsk} = -\varepsilon k_{rsk} F_{obs}$$
$$\tau_{rsk} = -\varepsilon k_{rsk} \tau_{obs}$$
$$F_{tgl} = \varepsilon \gamma k_{tgl} R(\pi/2) F_{obs}$$
$$\tau_{tgl} = r_f \times F_{tgl}$$

where $\varepsilon = exp(-k_{dcy}v_x)$, k_{dcy}=velocity decay constant, $\eta = -\hat{v}_x.\hat{F}_{obs}$, $\lambda = sgn(v_x)(\hat{v}_x\hat{F}_{tgl})(\hat{v}_x\hat{F}_{att})$, $\gamma = \begin{cases} rand[1,-1] \text{ if } v_x < v_{tan} \text{ and } \eta \leq \eta_{max} \\ sgn(\lambda) \text{ otherwise} \end{cases}$, $\hat{e}$=unit vector of e, η_{max}=maximum heading direction limit, k_{tgl}=proportional tangential gain, $R\left(\frac{\pi}{2}\right) = \begin{pmatrix} 0 & -1 \\ 1 & 0 \end{pmatrix}$=90° rotation matrix. The tangential force applies a small force from obstacles acting perpendicular to the vehicle velocity direction. The risk force reduces repulsive forces at low speeds. We deployed a four-wheeled Clearpath Robotics A200 Husky rover equipped with a single laser scanner to scan the local (indoor) environment and range data was transformed into forces and torques on the rover. The risk force and tangential force were applied to "shape" the standard potential field. RAVE was tested using the Husky all-terrain mobile robot operated through a ground floor circuit at Carleton University (Fig 6).
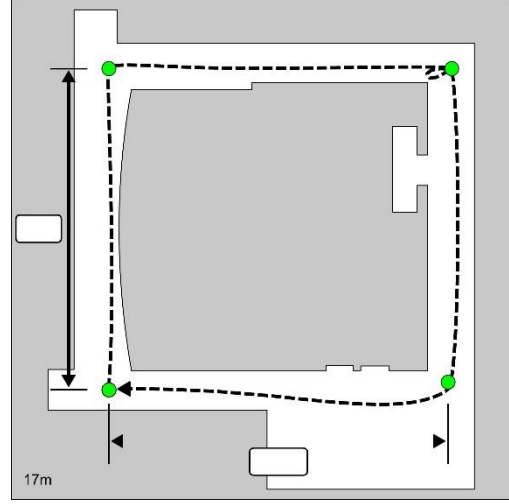
Figure 6. Carleton University closed circuit

The RAVE algorithm demonstrated successfully its effectiveness in cluttered conditions (Fig 7).
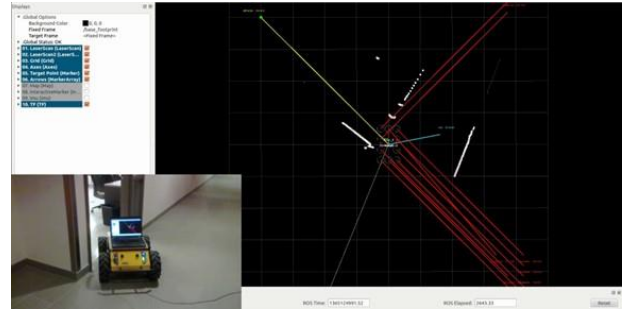
Figure 7. Husky rover negotiating narrow doorway

We further explored the limits of potential fields regarding rock-cluttered environments using simulated environments. Mars rock distribution models define the probability of rocks of diameter D [16]:

$$p(D) = ke^{-q(k)D}$$

where k=cumulative fractional area covered by rocks, k_{VL1}=0.069, k_{VL2}=0.176, k_{MPF}=0.187, k_{MER}=0.07, $q(k) = 1.79 + \left(\frac{0.152}{k}\right)$= exponent coefficient. The potential field was based on a polar representation of potential fields [17] (Fig 8):

$$\ddot{\phi} = \ddot{\phi}_g - \ddot{\phi}_{obs} - b\dot{\phi}$$

where $\dot{\phi}$=rover angular velocity, b=damping parameter, $\ddot{\phi}_g$=attractive angular acceleration imposed by the attractive goal, $\ddot{\phi}_{obs}$=repulsive angular acceleration imposed by the obstacle ensemble.
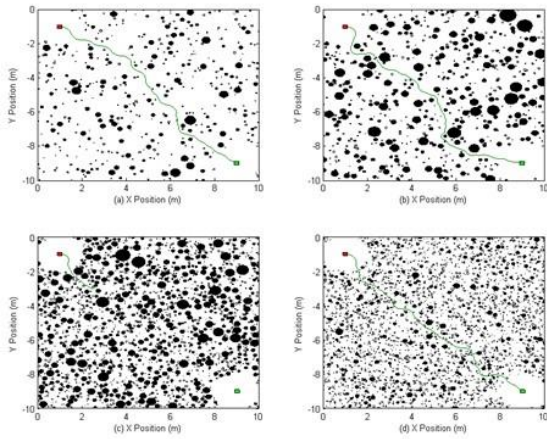
Figure 8. Simulated Mars rock distributions

Rover velocity is determined by the density of obstacles:

$$v = v_{max}e^{-k_v \Sigma |\ddot{\phi}_{obs,i}|} - \varepsilon$$

where k_v=velocity gain, ε=velocity resolution. Saturation of the velocity controller occurs when the obstacle density is too great causing the rover to stop. An example of unwanted velocity controller saturation occurs where the rover stopped before two obstacles of the rockfield even though there was sufficient space to squeeze through. This was due to the tuning of the velocity controller and the gap constant. This of course can be altered to permit free passage through the tighter obstacle configuration.

5. CONCLUSIONS

We have explored several crucial issues in enabling rover operations in subsurface mines on the Moon – slippage, visual navigation and path planning. Although we have encountered issues that arise in this application, we have not encountered any major showstoppers. Although we have restricted ourselves to exploring rover operations for pre-existing tunnel mines, we have not explored the excavation of such mining tunnels which represents a more challenging problem.

6. APPENDIX

Table 1. Lunar industrial ecology extracts a range of useful materials (emboldened oxides require further reduction processing to yield pure metals such as molten salt electrolysis [18])

RAW RESOURCE INPUTS

Ilmenite
$Fe^0 + H_2O$
$FeTiO_3 + H_2 \rightarrow \textbf{TiO}_2 + H_2O + Fe$ and $2H_2O \rightarrow 2H_2 + O_2$
$\uparrow$_____|
$2Fe + 1.5O_2 \rightarrow Fe_2O_3/Fe_2O_3.CoO$
$3Fe_2O_3 + H_2 \leftrightarrow Fe_3O_4 + H_2O$)

M-type Meteorites
$4Fe_2O_3 + Fe \leftrightarrow 3Fe_3O_4$)
W inclusions
Carbonyl process:
$Fe(CO)_5 \leftrightarrow 5CO + Fe$ (175°C/100 bar)
$Ni(CO)_4 \leftrightarrow 4CO + Ni$ (55°C/1 bar)
$Co_2(CO)_8 \leftrightarrow 8CO + 2Co$ (150°C/35 bar)
   S catalyst
$4FeS + 7O_2 \rightarrow \textbf{2Fe}_2\textbf{O}_3 + 4SO_2$
Troilite $SO_2 + H_2S \rightarrow 3S + H_2O$
$FeSe + Na_2CO_3 + 1.5O_2 \rightarrow \textbf{FeO} + Na_2SeO_3 + CO_2$
         KNO_3 catalyst $Na_2SeO_3 + H_2SO_4 \rightarrow Na_2O + H_2SO_4 + Se$
                          $\uparrow$_____|
                          $Na_2O + H_2O \rightarrow 2NaOH$

Lunar Orthoclase
$NaOH + HCl \rightarrow NaCl + H_2O$ (recycle)
$3KAlSi_3O_8 + 2HCl + 12H_2O \rightarrow KAl_3Si_3O_{10}(OH)_2 + 6H_4SiO_4 + 2KCl$
  orthoclase   illite   silicic acid (soluble silica $\rightarrow \textbf{SiO}_2 + H_2O$)
$2KAl_3Si_3O_{10}(OH)_2 + 2HCl + 3H_2O \rightarrow 3Al_2Si_2O_5(OH)_4 + 2KCl$
               kaolinite $KCl + NaNO_3 \rightarrow NaCl + KNO_3$ (recycled)

Lunar Anorthite
$CaAl_2SiO_8 + 4C \rightarrow CO + \textbf{CaO} + \textbf{Al}_2\textbf{O}_3 + 2Si$ at 1650°C
                $CaO + H_2O \rightarrow Ca(OH)_2$
                      $Ca(OH)_2 + CO_2 \rightarrow CaCO_3 + H_2O$
$CaAl_2SiO_8 + 5HCl + H_2O \rightarrow CaCl_2 + 2AlCl_3.6H_2O + \textbf{SiO}_2$
              $AlCl_3.6H_2O \rightarrow Al(OH)_3 + 3HCl + H_2O$ at 100°C
      $\uparrow$_____|
              $Al(OH)_3 \rightarrow \textbf{Al}_2\textbf{O}_3 + 3H_2O$ at 400°C $\rightarrow 2Al + Fe_2O_3$

Lunar Olivine
$3Fe_2SiO_4 + 2H_2O \rightarrow 2Fe_3O_4 + \textbf{3SiO}_2 + 2H_2O$
  fayalite   magnetite
$Mg_2SiO_4 + 4H_2O \rightarrow \textbf{2MgO} + SiO_2 + 4H_2O$
  forsterite $MgO + HCl \rightarrow MgCl_2 + H_2O$

MANUFACTURED PRODUCT OUTPUTS

$\rightarrow$ ferrofluidic sealing

$\rightarrow$ ferrite magnets
$\rightarrow$ magnetite at 350-750°C/1-2 kbar

$\rightarrow$ thermionic cathodic material

Iron alloy	Ni	Co	Si	C	W
$\rightarrow$ Tool steel				2%	9-18%
$\rightarrow$ Electrical steel			3%		
$\rightarrow$ Permalloy	80%				
$\rightarrow$ Kovar	29%	17%	0.2%	0.01%.	

$\rightarrow$ photosensitive Se

$\rightarrow$ kaolinite binder $\rightarrow$ porcelain

$\rightarrow$ CaO cathode coatings

$\rightarrow$ fused silica glass + FFC electrolyte

$\rightarrow 2Fe + Al_2O_3$ (thermite)
$\rightarrow$ AlNiCo hard magnets

$\rightarrow$ 3D Shaping binder (Sorel cement)
$\rightarrow$ 3D Shaping binder (Sorel cement)

Lunar Pyroxene

$Ca(Fe,Al)Si_2O_6 + HCl + H_2O \rightarrow Ca_{0.33}(Al)_2(Si_4O_{10})(OH)_2.nH_2O + H_4SiO_4 + CaCl_2 + Fe(OH)_3$

    augite   montmorillonite   silicic acid   iron hydroxide

$6MgSiO_3 + H_2O \rightarrow Mg_3Si_2O_5(OH)_4 + Mg_3Si_4O_{10}(OH)_2$ $\rightarrow$ dry lubricant talc

    enstatite   serpentine   talc

Lunar Volatiles

$CO + 0.5 O_2 \rightarrow CO_2$

                  $CO_2 + 4H_2 \rightarrow CH_4 + 2H_2O$ at 300ºC (Sabatier reaction) $\rightarrow CH_4 \rightarrow C + 2H_2$ at 1400ºC $\rightarrow$ steel additive/anode regeneration

                   Ni catalyst

    850ºC   250ºC

$CH_4 + H_2 \rightarrow CO + 3H_2 \rightarrow CH_3OH$ 350ºC

   Ni catalyst Al_2O_3 catalyst $CH_3OH + HCl \rightarrow CH_3Cl + H_2O$ 370ºC $+nH_2O$ (Rochow process)

                        Al_2O_3 catalyst $CH_3Cl + Si \rightarrow (CH_3)_2SiCl_2 \rightarrow ((CH_3)_2SiO)_n + 2nHCl \rightarrow$ silicone plastics/oils

$N_2 + 3H_2 \rightarrow 2NH_3$ (Haber-Bosch process)   ↑_____|

  Fe on $CaO+SiO_2+Al_2O_3$ catalyst

$4NH_3 + 5O_2 \rightarrow 4NO + 6H_2O$

      WC on Ni catalyst

          $3NO + H_2O \rightarrow 2HNO_3 + NO$ (Ostwald process)

       ↑_____|

$2SO_2 + O_2 \leftrightarrow 2SO_3$ (low temp)

          $SO_3 + H_2O \rightarrow H_2SO_4$

Earth-Supplied Salt-Derived Reagents

$2NaCl + CaCO_3 \leftrightarrow Na_2CO_3 + CaCl_2$ (Solvay process) $\rightarrow$ FFC electrolyte

                 350ºC/150 MPa

             $Na_2CO_3 + SiO_2(i) \leftrightarrow Na_2SiO_3 + CO_2$ $\rightarrow$ piezoelectric quartz

       1000-1100ºC   (40-80 day growth)

      $CaCO_3 \rightarrow$ **CaO** $+ CO_2$ (calcination)

$NaCl(s) + HNO_3(g) \rightarrow HCl(g) + NaNO_3(s)$ $\rightarrow$ recycled acid leach

Table 2. Lunar demandite of functional materials required for a spacecraft derivable from lunar resources [19]

Functionality (mass fraction)	Lunar-Derived Material
Tensile structures (25%)	Wrought iron Aluminium
Compressive structures (+50%)	Cast iron Regolith + binder
Elastic structures (trace)	Steel springs/flexures Silicone elastomers
Hard structures (3%)	Alumina
Thermal conductor straps (1%)	Fernico (e.g. kovar) Nickel Aluminum
Thermal radiators (3%)	Aluminium
Thermal insulation (3%)	Glass (SiO_2 fibre) Ceramics such as SiO_2
High thermal tolerance (4%)	Tungsten Alumina
Electrical conduction wire (7%)	Aluminium Fernico (e.g. kovar) Nickel
Electrical insulation (1%)	Glass fibre Ceramics (SiO_2, Al_2O_3 and TiO_2) Silicone plastics Silicon steel for motors
Active electronics devices (vacuum tubes) (12%)	Kovar Nickel Tungsten Fused silica glass
Magnetic materials for actuators (5%)	Ferrite Silicon steel Permalloy
Sensory transducers (5%)	Resistance wire Quartz Selenium
Optical structures (11%)	Polished nickel/aluminium Fused silica glass lenses
Lubricants (trace)	Silicone oils Water
Power system (20%)	Fresnel lens + thermionic conversion Flywheels
Combustible fuels (+250%)	Oxygen Hydrogen
Functionality (mass fraction)	Lunar-Derived Material
Tensile structures (25%)	Wrought iron Aluminium
Compressive structures (+50%)	Cast iron Regolith + binder
Elastic structures (trace)	Steel springs/flexures Silicone elastomers
Hard structures (3%)	Alumina
Thermal conductor straps (1%)	Fernico (e.g. kovar) Nickel Aluminum
Thermal radiators (3%)	Aluminium

Thermal insulation (3%)	Glass (SiO2 fibre) Ceramics such as SiO2
High thermal tolerance (4%)	Tungsten Alumina
Electrical conduction wire (7%)	Aluminium Fernico (e.g. kovar) Nickel
Electrical insulation (1%)	Glass fibre Ceramics (SiO2, Al2O3and TiO2) Silicone plastics Silicon steel for motors
Active electronics devices (vacuum tubes) (12%)	Kovar Nickel Tungsten Fused silica glass
Magnetic materials for actuators (5%)	Ferrite Silicon steel Permalloy
Sensory transducers (5%)	Resistance wire Quartz Selenium
Optical structures (11%)	Polished nickel/aluminium Fused silica glass lenses
Lubricants (trace)	Silicone oils Water
Power system (20%)	Fresnel lens + thermionic conversion Flywheels
Combustible fuels (+250%)	Oxygen Hydrogen

[10] Rosten E, Drummond T (2006) "Machine learning for high-speed corner detection" *Proc European Conf on Computer Vision*, 1-14

[11] Leuteneggar S, Chli M, Siegwart R (2011) "BRISK: binary robust invariant scalable keypoints" *Proc IEEE Int Conf Computer Vision*, 2548-2555

[12] Rublee E, Rabaud V, Konolige K, Bradski G (2011) "ORB: an efficient alternative to SIFT or SURF" *Proc IEEE Int Conf Computer Vision*, 2564-2571

[13] Sturm J, Engelhard N, Endres F, Burgard W, Cremers D (2012) "Benchmark for the evaluation of RGB-D SLAM systems" *Proc IEEE Int Conf Intelligent Robots & Systems*, 573-580

[14] Endres F, Hess J, Engelhard N, Sturm J, Cremers D, Burgard W (2012) "Evaluation of the RGB-D SLAM" *Proc IEEE Int Conf Robotics & Automation* **3** (5) 1691-1996

[15] Lynch B, Ellery A and Nitzsche F (2008) "Two-dimensional robotic vehicle path planning based on artificial potential fields" *Proceedings of CSME Forum*, Ottawa, Canada

[16] Golombek M and Rapp D (1997) "Size-frequency distributions of rocks on Mars and Earth analogue sites: implications for future landed missions," *J Geophysical Research* **102** (E2), 4117-4129

[17] Huang H, Fajen B, Fink J, Warren W (2006) "Visual navigation and obstacle avoidance using a steering potential function" *Robotics & Autonomous Systems* **54** (4), 288-299

[18] Ellery A, Mellor I, Wanjara P, Conti M (2022) "Metalysis FFC process as a strategic lunar in-situ resource utilisation technology" *New Space J* **10** (2), 224-238

[19] Ellery A (2022) "Lunar demandite – you gotta make this using nothing but that" *Proc ASCE Earth & Space Conf*, Colorado School of Mines, Denver, 743-758

7. REFERENCES

[1] Ellery A (2020) "Sustainable in-situ resource utilisation on the Moon" *Planetary & Space Science* **184** (4), 104870

[2] Yue Z, Johnson B, Monton D, Melosh H, Di K, Hu W, Liu Y (2013) "Projectile remains in central peaks of lunar impact craters" *Nature Geoscience* **6**, 435-437

[3] Wieczorek M, Weiss B, Steart S (2012) "Impactor origin for lunar magnetic anomalies" *Science* **335**, 1212-1215

[4] Collins G (2012) "Moonstruck magnetism" *Science* **335**, 1176-1177 Collins G (2012) "Moonstruck magnetism" *Science* **335**, 1176-1177

[5] Lindemann R, Voorhees (2005) "Mars exploration rover mobility assembly design, test and performance" *IEEE Int Conf Systems, Man and Cybernetics* **1**, 450–455

[6] Durrant-Whyte H, Bailey T (2006) "Simultaneous localization and mapping (SLAM): part 1 – essential algorithms" *IEEE Robotics & Automation Magazine* **13** (2), 99-110

[7] Julier S & Uhlmann J (2004) "Unscented filtering and nonlinear estimation" *Proc IEEE* **92** (3), 401-422

[8] Lowe G (2004) "SIFT – the scale invariant feature transform" *Int J Computer Vision* **60** (2), 91-110

[9] Bay H, Tuytelaars T, van Gool L (2006) "SURF: speeded up robust features" *Lecture Notes in Computer Science* **3951**, 404-417